

# Deep level defects and cation sublattice disorder in $\text{ZnGeN}_2$

Cite as: J. Appl. Phys. **127**, 135703 (2020); doi: [10.1063/1.5141335](https://doi.org/10.1063/1.5141335)

Submitted: 4 December 2019 · Accepted: 17 March 2020 ·

Published Online: 3 April 2020



Micah S. Haseman,<sup>1,a)</sup> Md Rezaul Karim,<sup>2</sup> Daram Ramdin,<sup>1</sup> Brenton A. Noesges,<sup>1</sup> Ella Feinberg,<sup>3</sup> Benthara Hewage Dinushi Jayatunga,<sup>4</sup> Walter R. L. Lambrecht,<sup>4</sup> Menglin Zhu,<sup>5</sup> Jinwoo Hwang,<sup>5</sup> Kathleen Kash,<sup>4</sup> Hongping Zhao,<sup>2,5</sup> and Leonard J. Brillson<sup>1,2</sup>

## AFFILIATIONS

<sup>1</sup>Department of Physics, The Ohio State University, Columbus, Ohio 43210, USA

<sup>2</sup>Department of Electrical and Computer Engineering, The Ohio State University, Columbus, Ohio 43210, USA

<sup>3</sup>Columbus School for Girls, Columbus, Ohio 43209, USA

<sup>4</sup>Department of Physics, Case Western Reserve University, Cleveland, Ohio 44106, USA

<sup>5</sup>Department of Materials Science and Engineering, The Ohio State University, Columbus, Ohio 43210, USA

<sup>a)</sup>Author to whom correspondence should be addressed: [haseman.2@osu.edu](mailto:haseman.2@osu.edu)

## ABSTRACT

III-nitrides have revolutionized lighting technology and power electronics. Expanding the nitride semiconductor family to include heterovalent ternary nitrides opens up new and exciting opportunities for device design that may help overcome some of the limitations of the binary nitrides. However, the more complex cation sublattice also gives rise to new interactions with both native point defects and defect complexes that can introduce disorder on the cation sublattice. Here, depth-resolved cathodoluminescence spectroscopy and surface photovoltage spectroscopy measurements of defect energy levels in  $\text{ZnGeN}_2$  combined with transmission electron microscopy and x-ray diffraction reveal optical signatures of mid-gap states that can be associated with cation sublattice disorder. The energies of these characteristic optical signatures in  $\text{ZnGeN}_2$  thin films grown by metal-organic chemical vapor deposition are in good agreement with multiple, closely spaced band-like defect levels predicted by density functional theory. We correlated spatially resolved optical and atomic composition measurements using spatially resolved x-ray photoelectron spectroscopy with systematically varied growth conditions on the same  $\text{ZnGeN}_2$  films. The resultant elemental maps vs defect spectral energies and intensities suggest that cation antisite complexes ( $\text{Zn}_{\text{Ge}}\text{-Ge}_{\text{Zn}}$ ) form preferentially vs isolated native point defects and introduce a mid-gap band of defect levels that dominate electron-hole pair recombination. Complexing of  $\text{Zn}_{\text{Ge}}$  and  $\text{Ge}_{\text{Zn}}$  antisites manifests as disorder in the cation sub-lattice and leads to the formation of wurtzitic  $\text{ZnGeN}_2$  as indicated by transmission electron microscopy diffraction patterns and x-ray diffraction reciprocal space maps. These findings emphasize the importance of growth and processing conditions to control cation place exchange.

Published under license by AIP Publishing. <https://doi.org/10.1063/1.5141335>

## I. INTRODUCTION

II-IV nitrides are a class of heterovalent, ternary materials composed of earth-abundant elements analogous to III-nitrides and constructed by replacing every group III atom with alternating group II and IV atoms. While the III-nitrides have received considerable attention for their potential in optoelectronics, fewer fundamental works have been carried out on II-IV-nitrides despite the potential advantages offered by these ternary semiconductors. Dual cation species and added complexity in the II-IV- $\text{V}_2$  crystal structure provide additional channels for bandgap tailoring, nonlinear optics,

defect engineering, and doping methods compared to III-nitrides.<sup>1,2</sup> Zinc-germanium-nitride ( $\text{ZnGeN}_2$ ) is a member of the II-IV- $\text{N}_2$  family predicted to have a very similar band structure to GaN with a good lattice match (1.1% lattice mismatch).<sup>3</sup> Moreover, the large valence band offset ( $\Delta E_v = 1.1$  eV)<sup>4</sup> and thus type-II heterojunction predicted for  $\text{ZnGeN}_2$  and GaN present opportunities for device architecture, notably in the design of InGa $\text{N}$ - $\text{ZnGeN}_2$  quantum wells with much improved efficiency as blue and green emitters, a result of shaping the hole wave function for greater overlap with the electron wavefunction.<sup>5</sup> The similarities to GaN, in both crystal

and electronic structures, and the ternary nature of  $\text{ZnGeN}_2$  make it a promising complement to the III–V family of nitrides in optoelectronics.

$\text{ZnGeN}_2$  was first synthesized in the 1970s via high pressure powder synthesis,<sup>6</sup> but only recently have high quality  $\text{ZnGeN}_2$  thin films been realized.<sup>7–9</sup> Several experimental reports have targeted the  $\text{ZnGeN}_2$  crystal structure, emphasizing the role of lattice ordering/disordering and the transition from orthorhombic to wurtzite  $\text{ZnGeN}_2$ .<sup>10–12</sup> Additional studies have focused on determination of bandgap energy, which has been reported to range from 3.0 to 3.5 eV<sup>12,13</sup> via absorption/reflection measurements and to be 3.4 eV via temperature-dependent photoluminescence, in good agreement with theory.<sup>3,14–16</sup> However, the role of defects on the optical and electrical properties of  $\text{ZnGeN}_2$  is relatively unexplored. While theoretical studies have provided thermodynamically stable gap state energy levels for  $\text{ZnGeN}_2$  native point defects,<sup>17–20</sup> analysis of their features has been restricted to analogies with GaN. In this work, we used depth-resolved cathodoluminescence spectroscopy (DRCLS) and surface photovoltage spectroscopy (SPS) to identify optical transitions in high quality  $\text{ZnGeN}_2$  thin films that correspond to energy levels predicted by density function theory (DFT) for both native point defects and defect complexes. We used spatially resolved x-ray photoelectron spectroscopy (XPS) to generate chemical maps across  $\text{ZnGeN}_2$  surfaces and to compare variations in elemental stoichiometry with corresponding spatially resolved DRCLS variations in deep level defect energies and relative densities. Combined with measurements of transmission electron microscopy (TEM) diffraction patterns and x-ray diffraction (XRD) reciprocal space maps (RSMs), these experimental observations suggest that cation nearest neighbor's place exchange occurs and that  $\text{Zn}_{\text{Ge}}\text{--Ge}_{\text{Zn}}$  antisite complexes, predicted theoretically, develop preferentially over the isolated native point defects, forming multiple, closely spaced band-like defect levels that dominate electron–hole pair recombination.

## II. EXPERIMENTAL

The  $\text{ZnGeN}_2$  thin films in this work were grown on *c*- and *r*-plane sapphire by metal–organic chemical vapor deposition (MOCVD) using diethylzinc (DEZn), germane ( $\text{GeH}_4$ ), and ammonia ( $\text{NH}_3$ ) as precursors for Zn, Ge, and N, respectively. The films were grown at 650 °C with a total reactor pressure of 500 Torr and a DEZn/ $\text{GeH}_4$  molar flow rate ratio of 25. X-ray diffraction (XRD)  $2\theta$ – $\omega$  scans confirmed that the films are single crystalline. A detailed study on MOCVD growth, crystallinity, and surface morphological properties of the films can be found in Ref. 7. DRCLS employs a glancing incidence electron gun in an ultrahigh vacuum (UHV) chamber with a  $\text{CaF}_2$  focusing lens inside the chamber coupled with a fiber optic cable outside the chamber connected to an Oriel monochromator and a CCD detector. SPS employs a non-contact atomic force microscope (AFM) probe tip in the Kelvin Probe Force Microscopy (KPFM) mode to measure the change in charge potential difference between the tip and the sample surface due to photo-stimulated population or depopulation transitions, providing identification of energy levels within the bandgap and with respect to the valence ( $E_v$ ) or conduction ( $E_c$ ) band.<sup>21–23</sup> Our XPS uses an Al  $K\alpha$  source to provide spatially resolved Zn, Ge, and N elemental maps across sample surfaces to track changes in Zn/Ge

ratio. Convergent beam electron diffraction (CBED) patterns were captured using a ThermoFisher probe-corrected STEM operated at 300 kV. X-ray diffraction measurements were performed using a Bruker D8 Discover XRD with a Cu  $K\alpha$  source.

## III. RESULTS

Figures 1(a) and 1(b) display representative DRCL spectra for  $\text{ZnGeN}_2$  on *c*- and *r*-plane sapphire using an electron beam with energy  $E_B = 0.5$  keV. Monte Carlo simulations modeling the depth-dependence of electron–hole (e–h) pair generation provide a maximum excitation depth ( $R_B$ ) of  $\sim 10$  nm below the free surface for  $E_B = 0.5$  keV (Fig. S1 in the [supplementary material](#)). Figure 1 shows no emission from conduction-to-valence band (e.g., bandgap) recombination. In fact, nearly all of the electron–hole (e–h) pair recombination is dominated by mid-gap transitions centered at  $\sim 1.7$ , 1.9, and 2.2 eV. We increased  $E_B$  from 0.5 keV to 5.0 keV incrementally to probe from the  $\text{ZnGeN}_2$  surface ( $R_B = 10$  nm) to the film/substrate interface ( $R_B = 200$  nm). This enables probing possible variations in defect density that may develop during film growth. Additionally, recombination centers such as vacancies and voids arising from strain and interfacial diffusion may appear at film interfaces with characteristic spectral signatures. However, Fig. 1(c) that shows the DRCLS depth profile reveals relatively uniform films with little to no variation as a function of depth. Our highest accelerating voltage ( $E_{B, \text{max}} = 5.0$  keV) limits our probing deeper through the interface and into the substrate. The consistency in cathodoluminescence (CL) as  $R_B$  approaches the interface may suggest that potential effects of strain are minimal or perhaps localized, extending just a few nanometers into the film.

We used SPS to identify the positions of the energy levels within the bandgap. Here, the work function difference, recorded as a change in contact potential difference ( $\Delta\text{cpd}$ ) between the non-contact AFM tip and the sample surface, indicates how the Fermi level ( $E_F$ ) varies with photo-population and depopulation of states and thus the degree of band bending within the surface space charge region. A representative spectrum for  $\text{ZnGeN}_2$  on *c*-sapphire in Fig. 2 shows the onsets of photo-stimulated population and depopulation at energies that are well below the expected bandgap of  $E_G \sim 3.5$  eV and hence roughly near the middle of the bandgap. Based on the *n*-type character of  $\text{ZnGeN}_2$  known for these films,<sup>7</sup> the positive (upward)  $\Delta\text{cpd}$  slope changes at 1.55 and 1.8 eV correspond to the onsets of photo-stimulated depopulations from gap states to  $E_c$ .<sup>21,22</sup> Likewise, transitions from  $E_v$  into a gap state occur at negative slope changes in  $\Delta\text{cpd}$  at energies of 1.75 and 2.0 eV. The shoulder at approximately 3.5 eV represents photo-flattening at the  $\text{ZnGeN}_2$  bandgap. This is in close agreement with the measured bandgap of 3.4 eV via photoluminescence excitation (PLE) for  $\text{ZnGeN}_2$  films grown under similar conditions.<sup>7</sup>

Figure 3(a) illustrates in blue the onset energies and conduction or valence band nature of the photo-stimulated onsets as shown in Fig. 2. In addition, Fig. 3(a) shows in red the CL emission energies measured in Fig. 1, which display close correspondence with the SPS energies. Figure 3(a) demonstrates good agreement between the two techniques and confirms that deep level emissions dominate the optical processes in these  $\text{ZnGeN}_2$  specimens. The

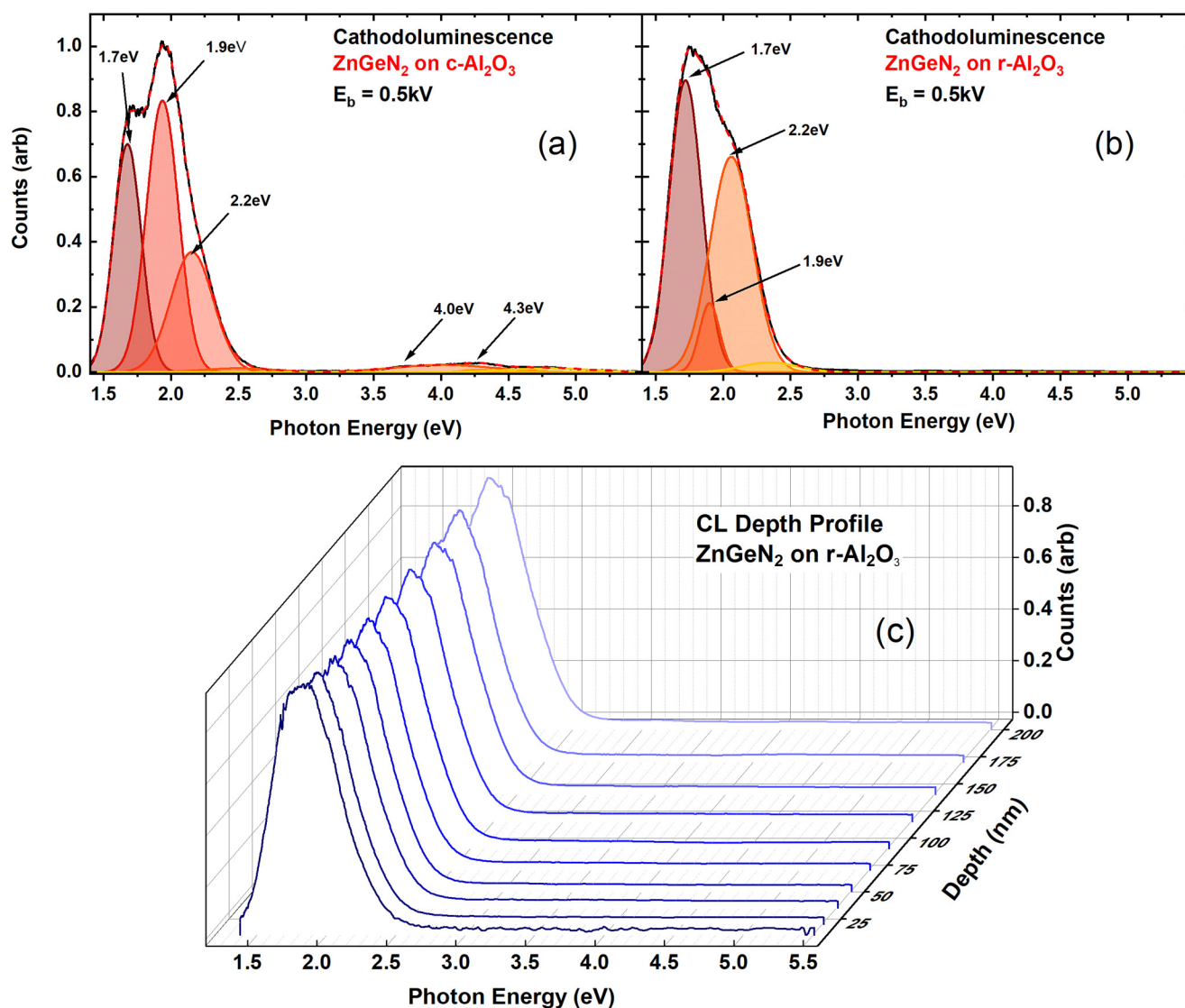


**FIG. 1.** Deconvolved cathodoluminescence (CL) spectra show three characteristic ZnGeN<sub>2</sub> mid-gap peaks for (a) c-Al<sub>2</sub>O<sub>3</sub> and (b) r-Al<sub>2</sub>O<sub>3</sub> substrates. (c) CL depth profile shows relative uniformity with depth.

energy levels indicated by CL and SPS transitions suggest a set of three energy levels in a band ranging from 1.7 to 2.2 eV above  $E_v$ .

Figure 3(b) illustrates energy levels for various native point defects in ZnGeN<sub>2</sub> predicted by two DFT group calculations, using a local density approximation (LDA) +  $U^{18}$  vs a hybrid functional approach.<sup>20</sup> In general, there is good agreement between these two methods. The theoretical energies shown correspond to the energies at which specific point defects change their charge states in plots of heats of formation  $\Delta H_F$  vs  $E_F$  position inside the bandgap. For example, the highest energy at which the Zn<sub>Ge</sub> antisite changes charge state ( $-1/-2$ ) occurs at  $E_F - E_v = 1.4$  eV for Zn-rich conditions.<sup>20</sup> Figure 3(b) shows that the most thermodynamically stable

point defects—Zn<sub>Ge</sub>, V<sub>Zn</sub>, and V<sub>N</sub>—all lie at energies deep within the ZnGeN<sub>2</sub> bandgap but outside the mid-gap range of energy levels measured experimentally.

Not shown is the 1.8 eV V<sub>Ge</sub> transition since this defect is energetically unfavorable.<sup>18</sup> Both Lyu *et al.*<sup>18</sup> and Adamski *et al.*<sup>20</sup> suggested that Zn<sub>Ge</sub> and V<sub>Zn</sub> are the most stable individual native point defects for n-type material in both Zn-rich and Zn-poor environments. However, the agreement between these point defect energy levels and those observed experimentally is not strong. Alternatively, consideration of the band structure and thermodynamics of cation antisite complexes (Zn<sub>Ge</sub>-Ge<sub>Zn</sub>) can account for the transition levels observed via CL and SPS. Adamski *et al.*<sup>20</sup>

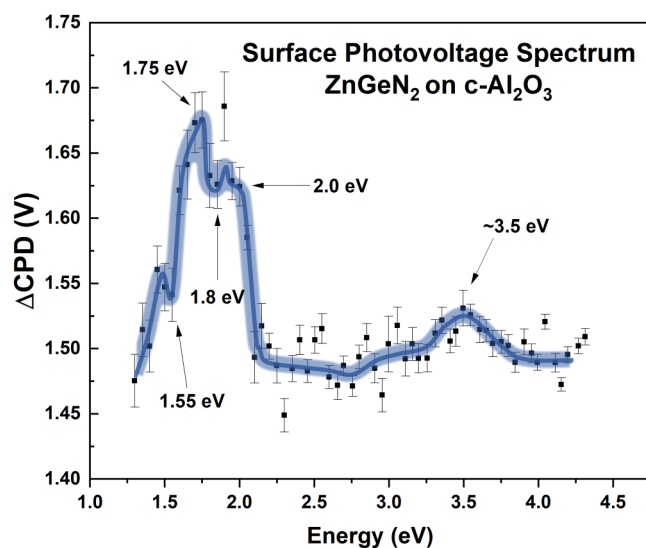


**FIG. 2.** SPS spectra of  $\text{ZnGeN}_2$  on  $c\text{-Al}_2\text{O}_3$  showing strongest  $\Delta\text{cpd}$  photo-depopulation and population onsets at 1.55–2.0 eV, all near the middle of the bandgap. The blue band serves as a guide to the eye.

calculated the energy of formation for a  $\text{Zn}_{\text{Ge}}\text{-Ge}_{\text{Zn}}$  complex and found a low energy of formation of about 2.0 eV in the neutral charge state over most of the gap, lower than the sum of the energies of the separated  $\text{Zn}_{\text{Ge}}$  and  $\text{V}_{\text{Zn}}$  defects. Likewise, Lyu *et al.*<sup>18</sup> showed that negatively charged  $\text{Zn}_{\text{Ge}}$  and positively charged  $\text{Ge}_{\text{Zn}}$  are electrostatically attracted and bind by 0.56 eV per pair compared with their separate, noninteracting defects. Such defect complexes, which result from swapping Zn and Ge locally, were also studied as “exchange defects” by Skachkov *et al.*<sup>24</sup> and were shown to lead to a mid-gap band of closely spaced defect levels which moves progressively deeper (higher above the VBM) with increasing octet-rule violating tetrahedra around nearby N (i.e., 1 Zn and 3 Ge instead of 2 Zn and 2 Ge). A similar conclusion was reached

by Lany *et al.* in their study of such defects in  $\text{ZnSnN}_2$ .<sup>25</sup> Figure 3(c) depicts this predicted intermediate band in  $\text{ZnGeN}_2$  for local swaps of Zn and Ge. This band is approximately mid-gap and is in good agreement with the transition levels in Fig. 3(a).

The thermodynamic stability of individual  $\text{ZnGeN}_2$  native point defects depends strongly on Zn stoichiometry according to theoretical predictions.<sup>18,20</sup> In an attempt to distinguish between the different native point defects and the cation antisite complexes, we carried out DRCLS measurements as a function of elemental stoichiometry across the same individual  $\text{ZnGeN}_2$  surfaces. We grew 200 nm thick  $\text{ZnGeN}_2$  films on  $c$ - and  $r$ -plane sapphire (as in Ref. 7) and varied the stoichiometry laterally via thermal gradient across the substrate; the disparity in cation vaporization pressures led to a reduction in the Zn/Ge ratio for elevated temperatures and a relative increase in the cation ratio at lower temperatures. The Zn/Ge ratio was likewise varied as a function of depth by attenuating the Zn flow during the last 50 nm of growth. We tracked the stoichiometric variations along the thermal gradient via spatially resolved XPS. Figure 4(a) illustrates the spatial geometry for these XPS measurements. The CL spectra in Fig. 4(b) were acquired with a beam energy of 0.5 keV, with an excitation depth ( $R_B$ ) of just 10 nm below the surface, comparable to the depth sensitivity of the XPS core levels probed. As no emission was observed above 3.0 eV, the CL grating was rotated to better resolve the mid-gap regime.

Table I shows absolute elemental compositions for each of the film's constituents as well as the variation in the measured [Zn]:[Ge] at ratio. There is substantial variation in the Zn/Ge ratio between cooler regions where [Zn]:[Ge] = 1.21 and hotter regions of the same surface where [Zn]:[Ge] = 0.76. We obtained nearly identical results for  $\text{ZnGeN}_2$  grown on  $c$ -sapphire (Table S1 in the supplementary material). XPS survey spectra as well as  $\text{Ge}2p$ ,  $\text{Zn}2p$ , and  $\text{N}1s$  core level spectra are given in Fig. S2 in the supplementary material. Energy dispersive x-ray spectroscopy (EDX) graphs given in Fig. S3 in the supplementary material confirm that C and O in Table I reside solely on the sample surface and do not extend into the films.

Surprisingly, the CL surface spectra exhibit only small changes compared with these large stoichiometric variations across the same  $\text{ZnGeN}_2$  surfaces. Likewise, the DRCL spectra in Fig. 4(c) are very uniform despite the targeted stoichiometric variation. Figure 5

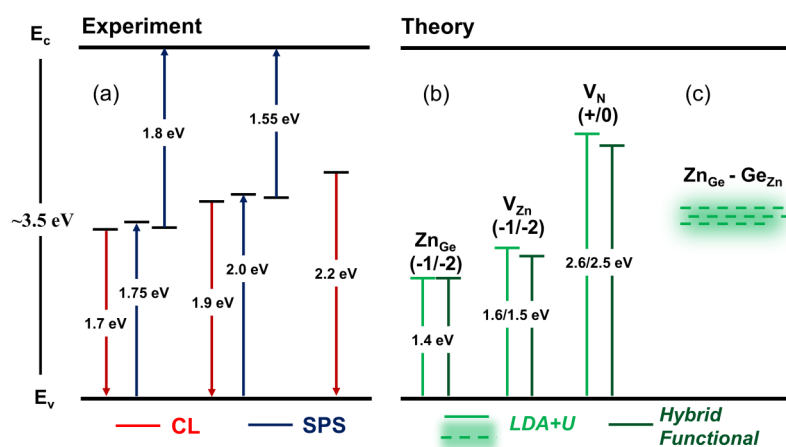


**FIG. 3.** (a) CL (red) and SPS (blue) optical transition measured experimentally show good agreement between luminescence and electrostatic techniques. (b) Mid-gap transition levels obtained theoretically (LDA +  $U$ <sup>20</sup> in green and Hybrid Functional<sup>16</sup> in dark green). (c) Intermediate defect band of levels originating from  $\text{Zn}_{\text{Ge}}\text{-Ge}_{\text{Zn}}$  antisite complexes predicted theoretically via LDA.<sup>24</sup>



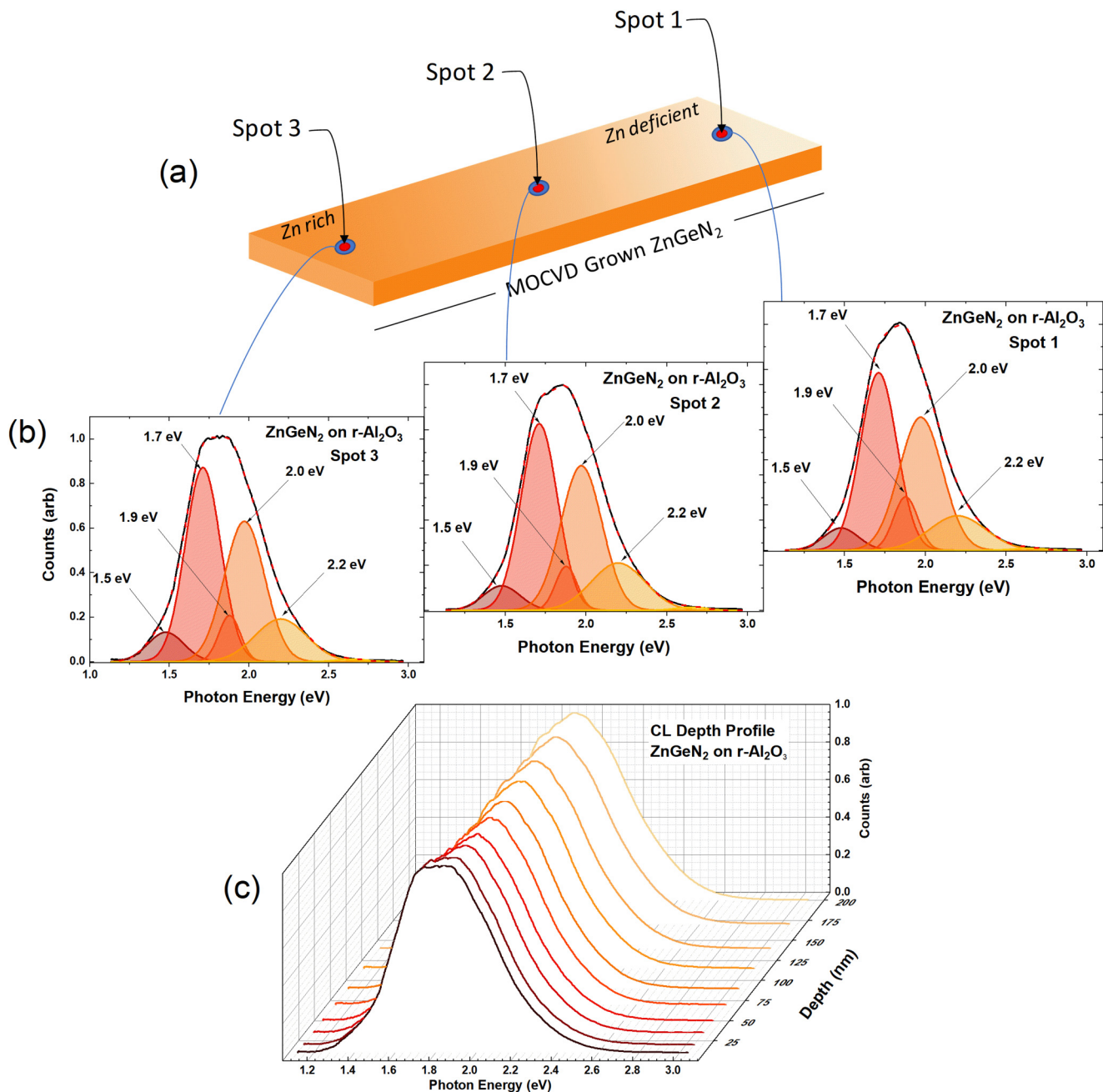


**FIG. 4.** (a) Schematic illustration of a ZnGeN<sub>2</sub> epilayer with variation in Zn composition. (b) Surface CL spectra corresponding to each measurement region. (c) DRCL spectra for spot 1. No significant differences in the spectra are apparent despite large differences in composition.

displays the variation in the CL peak area for each of the deconvolved peaks shown in Fig. 4. These spectra are normalized by the total peak area and plotted vs [Zn]:[Ge] ratios obtained via XPS. Little change in CL peak areas is observed when plotted against the large range of cation stoichiometries.

Zn<sub>Ge</sub> and to a lesser extent V<sub>Zn</sub><sup>18</sup> are the most thermodynamically stable native point defects that could form in both Zn-rich and Zn-poor regions. Their densities, however, would be sensitive to even small changes in cation stoichiometry. The near uniformity in the cathodoluminescence energies and intensities as the Zn/Ge

**TABLE I.** ZnGeN<sub>2</sub> film composition obtained via XPS as a function of thermal gradient from hotter (spot 1) to cooler (spot 3) regions of growth.

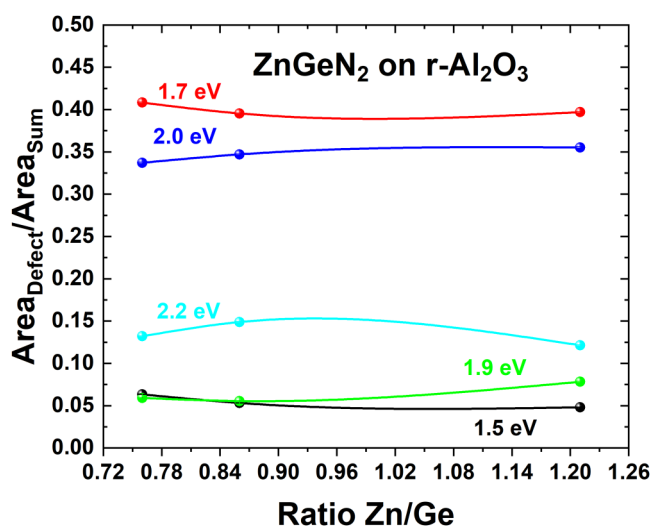
Spot	Stoichiometric % for 200 nm ZnGeN <sub>2</sub> on r-Al <sub>2</sub> O <sub>3</sub>						[Zn]:[Ge]
	C	O	Al	N	Zn	Ge	
1	15.5 ± 0.3	25.1 ± 0.9	<0.1	31.1 ± 0.4	12.2 ± 0.1	16 ± 0.2	0.76 ± 0.01
2	15.5 ± 0.3	28 ± 0.8	<0.1	28.7 ± 0.5	13 ± 0.1	15 ± 0.2	0.86 ± 0.01
3	15.5 ± 0.3	24.3 ± 1.2	<0.1	34.8 ± 0.5	14.8 ± 0.2	12.2 ± 0.2	1.21 ± 0.02

ratio varies would thus be unusual for the given cation related point defects. This consistency in CL, despite large stoichiometric variation, suggests that the mid-gap transitions are likely not due to isolated native point defects. On the other hand, the formation of Zn<sub>Ge</sub>-Ge<sub>Zn</sub> complexes is also expected in both Zn-rich and Zn-poor regions. Zn<sub>Ge</sub> acceptors, being the most thermodynamically favorable isolated defect in Zn-rich regions, likely complex with available Ge<sub>Zn</sub> donors to preserve local charge neutrality.<sup>20</sup> In Zn-poor regions, theory shows that the energies of formation for both Zn<sub>Ge</sub> and V<sub>Zn</sub> increase, i.e., become less energetically favorable, as E<sub>F</sub> moves toward E<sub>v</sub>. In fact, as the Fermi level rises to E<sub>v</sub> + 2.7 eV, the Zn<sub>Ge</sub>-Ge<sub>Zn</sub> complex becomes the most thermodynamically stable defect, with an energy of formation lower than the isolated point defects including the Ge<sub>Zn</sub><sup>2+</sup> antisite.<sup>20</sup> This prediction is in excellent agreement with the values for E<sub>F</sub> we obtain via XPS valence measurements, which puts E<sub>F</sub> between 2.64 and 2.76 eV (Fig. S4 in the [supplementary material](#)). Based on the calculated thermodynamics, the cation antisites preferentially complex with their respective counterparts in both Zn-rich and Zn-poor regimes. As a result, Zn<sub>Ge</sub>-Ge<sub>Zn</sub> antisite complexes are likely the dominant defect throughout these ZnGeN<sub>2</sub> films even as the stoichiometry is varied laterally (due to thermal gradient) and depth-wise (due to Zn flow attenuation). Theoretical predictions by Skachkov *et al.*<sup>24</sup> show that antisite complexes can

form a triplet of closely spaced defect levels near mid-gap as in Fig. 5 of Ref. 24. As shown in Fig. 3, these states can be considered an intermediate band within the gap that dominates electron-hole recombination and that could explain why the CL is independent of XPS-measured cation stoichiometries. Both [Zn]:[Ge] ratios and valence band variations observed with spatially localized XPS as well as the relatively uniform CL energies and intensities are all consistent with the formation of Zn<sub>Ge</sub>-Ge<sub>Zn</sub> complexes throughout the films.

This complexing of Zn<sub>Ge</sub> and Ge<sub>Zn</sub> antisites should manifest as disorder in the cation sublattice and lead to the wurtzite phase of ZnGeN<sub>2</sub> rather than the ordered, orthorhombic phase of ZnGeN<sub>2</sub>.<sup>15,19</sup> Here, disorder in the Zn and Ge sublattices brought on by the formation of Zn<sub>Ge</sub> and Ge<sub>Zn</sub> defects would on average restore the sixfold hexagonal symmetry of the wurtzite lattice. This is evidenced in both XRD reciprocal space maps (RSMs) and TEM diffraction patterns as shown in Figs. 6(a) and 6(b), respectively.

In orthorhombic ZnGeN<sub>2</sub>, ordering on the cation sublattice can split certain 2θ-ω peaks in the XRD of the parent wurtzite structure.<sup>26</sup> However, the degree of this disorder is difficult to determine from the diffraction patterns alone. For example, Quayle *et al.*<sup>15</sup> noted that wurtzite-like (disordered) diffraction spectra can be generated by both random stacking of two octet-rule-preserving structures as well as a fully random cation distribution. Furthermore, the intensity of the degeneracy splitting in diffraction peaks is dependent on atomic form factors; the predicted diffraction intensities for ZnGeN<sub>2</sub> are roughly an order of magnitude lower than for similar ternary nitrides like ZnSnN<sub>2</sub>.<sup>15</sup> Such peak splitting is readily visible for powder materials,<sup>27</sup> whereas XRD reciprocal space maps (RSMs) can be employed for single crystalline samples.<sup>28</sup> One example is the wurtzite (10-11) peak, which is sixfold symmetric about the c-axis and is expected to split into orthorhombic (121) and (201) peaks when the cation sublattice is ordered. Both orthorhombic planes are tilted by ~62° with respect to the c-plane, but their 2θ positions are slightly different at 36.382° and 36.842°. This leads to a systematic shift in the 2θ peak position when the sample is rotated by an angle Φ around the out-of-plane vector.<sup>28</sup> The reciprocal space map for ZnGeN<sub>2</sub> as shown in Fig. 6(a) was performed on a sample grown on c-sapphire under similar conditions as those used for DRCLS and XPS measurements with a Zn/Ge ratio of ~1, approximating the Zn-rich/Zn-poor crossover point of the films described above. The growth direction of the sample is along the c-axis.<sup>7</sup> Figure 6(a) shows the XRD 2θ-ω scan profiles from 2θ = 35.5°–38° for six Φ positions separated by 60° with the sample tilted by 62°. In an ordered ZnGeN<sub>2</sub> sample, two of the six peaks would correspond to the (121) plane and would be at slightly smaller 2θ positions with respect to the four (201) peaks. However, no systematic shift in the 2θ peak position is

**FIG. 5.** Surface CL peak area shown in Fig. 4 normalized by the total peak area, plotted vs [Zn]/[Ge] at ratios obtained via XPS.

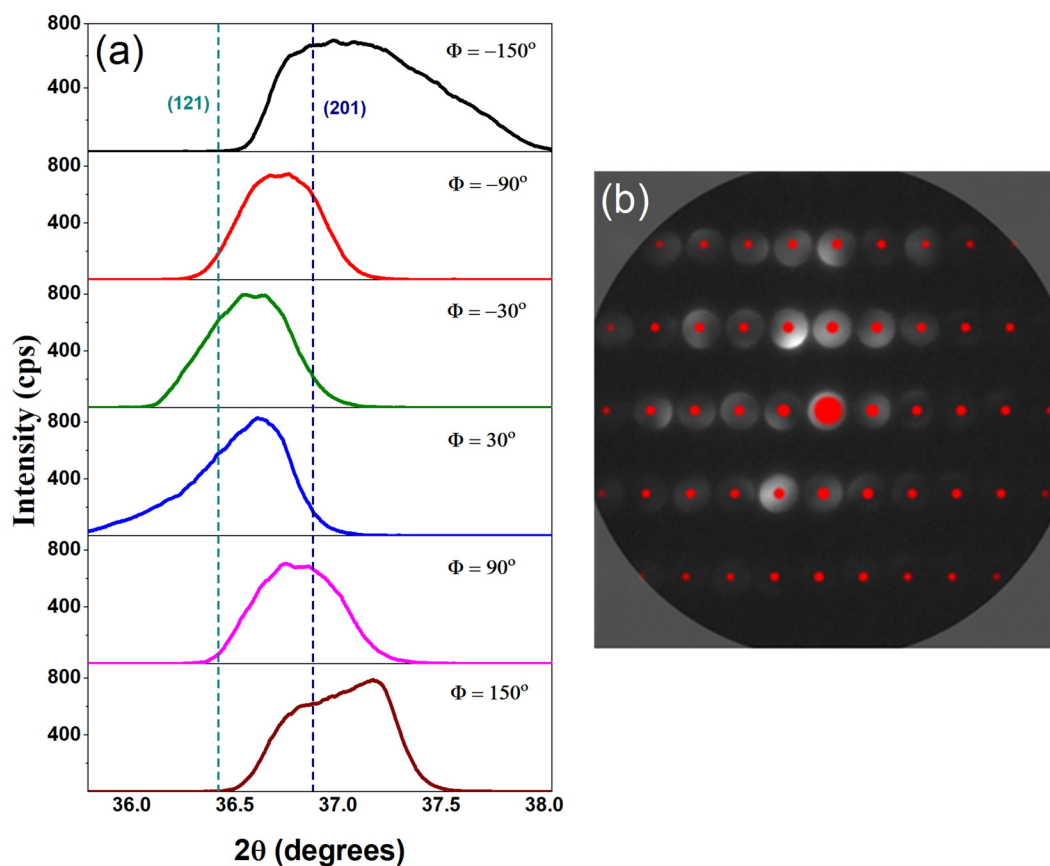


**FIG. 6.** (a) XRD  $2\theta$ - $\omega$  scan profiles for  $2\theta = 35.5^\circ$ – $38^\circ$  for six  $\Phi$  positions, where  $\Phi$  refers to the rotation of the sample around the out-of-plane vector. The observed peaks correspond to the wurtzite (10–11) planes. Light green and dark blue dashed lines denote the calculated positions of orthorhombic (121) and (201) peaks, respectively. (b) Experimental CBED pattern (white) with the calculated wurtzite pattern (red) overlaid.

observed in Fig. 6(a). The apparent cyclic shift from  $\Phi = -150^\circ$  (top panel) to  $\Phi = 150^\circ$  (bottom panel) is caused by the instrument alignment rather than any peak splitting. The wurtzitic structure was further confirmed by convergent beam electron

diffraction (CBED) patterns shown in Fig. 6(b) for stoichiometric  $\text{ZnGeN}_2$ . The experimental CBED pattern (white disks) was best matched with simulated TEM diffraction (red disks) when assuming a cation disordered wurtzite structure.

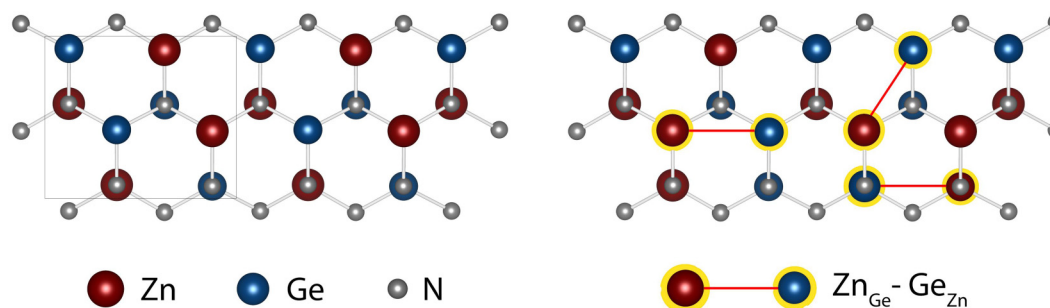


**FIG. 7.**  $\text{ZnGeN}_2$  orthorhombic lattice before (a) and after (b) place exchange.

#### IV. DISCUSSION

In the orthorhombic phase of  $\text{ZnGeN}_2$  as shown in Fig. 7, the atomic positions of the cations in the II–IV-nitride are shifted with respect to the wurtzite structure of the parent III-nitrides, resulting in a shorter Ge–N bond compared to the Zn–N bond and thus an orthorhombic unit-cell. The wurtzitic form of  $\text{ZnGeN}_2$  can then be considered as a disordered cation sublattice with  $\text{Zn}_{\text{Ge}}\text{--Ge}_{\text{Zn}}$  complexes [shown in Fig. 7(b)], a product of this disorder. LDA-DFT predicts that place exchanges can introduce multiple, closely spaced levels in the  $\text{ZnGeN}_2$  bandgap. Depending on their density of states, such states would then act as efficient recombination centers for free electron–hole pairs.<sup>24</sup> In high enough concentration, these states could form a partially filled broadened defect band within the bandgap, i.e., an intermediate band that could lead to recombination with both the VBM and CBM. The energy level positions calculated by Lyu *et al.* and Adamski *et al.* for these  $\text{Zn}_{\text{Ge}}$  and  $\text{Ge}_{\text{Zn}}$  levels appear to lie near mid-gap, while Adamski *et al.* have calculated the +/0 transition level for  $\text{Zn}_{\text{Ge}}\text{--Ge}_{\text{Zn}}$  complexes to lie  $\sim 0.5$  eV above the valence band. The threefold multiplicity of these predicted states for multiple cation place exchange in near proximity, their relatively close energy level spacing near mid-gap that we measure experimentally, and their distinct energy level differences from those predicted theoretically for isolated native point defects provide strong evidence for Zn–Ge place exchange and  $\text{Zn}_{\text{Ge}}\text{--Ge}_{\text{Zn}}$  defect complex formation.

#### V. CONCLUSIONS

We showed that the spectral features in these MOCVD-grown  $\text{ZnGeN}_2$  thin films are dominated by mid-gap transitions consistent with an intermediate band predicted by theory arising from the complexing of cation antisites. Future work of our group is geared toward further improving the growth and processing procedures to either suppress or enhance these cation disorder related defects. Previous results of vapor–liquid–solid growth in Ref. 10 indicate that cation ordering can be achieved at higher growth temperatures, but the road to realize this, as well as precise stoichiometry control in MOCVD, is not yet clear and will require further work. Zn/Ge cation ratios acquired via spatially resolved XPS provide evidence for preferential formation of  $\text{Zn}_{\text{Ge}}\text{--Ge}_{\text{Zn}}$  antisite complexes compared to isolated point defects, attributed to lower energies of formation and the preservation of local charge neutrality. TEM diffraction and XRD reciprocal space maps provide additional evidence of  $\text{Zn}_{\text{Ge}}\text{--Ge}_{\text{Zn}}$  complexes via cation sublattice disordering and are consistent with the wurtzite phase of  $\text{ZnGeN}_2$ . Alternatively, promoting the formation of a band of defect states near mid-gap could be useful to strongly decrease the optical absorption threshold energy in nitride heterostructures. These findings emphasize the importance of growth conditions to control cation place exchange. This work suggests that the control of antisite complexing is central to the growth of ordered, orthorhombic  $\text{ZnGeN}_2$  for use in advanced nitride-based optoelectronic applications.

#### SUPPLEMENTARY MATERIAL

See the [supplementary material](#) for Monte Carlo simulations modeling the depth-dependence of electron–hole (e–h) pair generation

in  $\text{ZnGeN}_2$  (Fig. S1); spatially resolved XPS table of stoichiometries for  $\text{ZnGeN}_2$  on  $\text{c-Al}_2\text{O}_3$  (Table S1); as well as core level region scans and survey spectra (Fig. S2), EDX analysis of Zn-rich and Zn-poor films (Fig. S3), and Fermi level extrapolations from XPS valence level region scans (Fig. S4).

#### ACKNOWLEDGMENTS

This work was supported by the National Science Foundation (NSF) under Grant Nos. DMREF:SusChEM:-1533957 (M.R.K., B.H.D.J., H.Z., W.R.L.L., and K.K.), DMR-18-00130 (L.J.B. and M.S.H.), and DMR-14-20451 (B.A.N.), and the Department of Energy under Grant No. DE-EE0008718 (M.R.K., B.H.D.J., K.K., and H.Z.). M.R.K., H.Z., M.Z., and J.H. also acknowledge support from the Seed Grant from the Institute for Materials Research at the Ohio State University and the Center for Emergent Materials, an NSF-funded MRSEC Award under No. DMR-1420451.

#### REFERENCES

- W. R. L. Lambrecht and A. Punya, *III-Nitride Semiconductors and Their Modern Devices* (Oxford University Press, 2013), pp. 519–585.
- S. Lyu and W. R. L. Lambrecht, *Phys. Rev. Mater.* **2**, 124602 (2018).
- A. Punya, W. R. L. Lambrecht, and M. Van Schilfgaarde, *Phys. Rev. B* **84**, 165204 (2011).
- A. P. Jaroenjittichai, S. Lyu, and W. R. L. Lambrecht, *Phys. Rev. B* **96**, 165204 (2017).
- L. Han, K. Kash, and H. Zhao, *J. Appl. Phys.* **120**, 103102 (2016).
- M. Wintenberger, M. Maunaye, and Y. Laurent, *Mater. Res. Bull.* **8**, 1049 (1973).
- M. R. Karim, B. H. D. Jayatunga, Z. Feng, K. Kash, and H. Zhao, *Cryst. Growth Des.* **19**, 4661 (2019).
- L. D. Zhu, P. H. Maruska, P. E. Norris, P. W. Yip, and L. O. Bouthillette, *MRS Internet J. Nitride Semicond. Res.* **4**, 149 (1999).
- T. Misaki, K. Tsuchiya, D. Sakai, A. Wakahara, H. Okada, and A. Yoshida, *Phys. Status Solidi C* **0**, 188 (2002).
- E. W. Blanton, K. He, J. Shan, and K. Kash, *J. Cryst. Growth* **461**, 38 (2017).
- S. Kikkawa and H. Morisaka, *Solid State Commun.* **112**, 513 (1999).
- R. Viennois, T. Taliercio, V. Potin, A. Errebah, B. Gil, S. Charar, A. Haidoux, and J. C. Tédénac, *Mater. Sci. Eng. B* **82**, 45 (2001).
- M. Shang, J. Wang, J. Fan, H. Lian, Y. Zhang, and J. Lin, *J. Mater. Chem. C* **3**, 9306 (2015).
- K. Du, C. Bekele, C. C. Hayman, J. C. Angus, P. Pirouz, and K. Kash, *J. Cryst. Growth* **310**, 1057 (2008).
- P. C. Quayle, E. W. Blanton, A. Punya, G. T. Junno, K. He, L. Han, H. Zhao, J. Shan, W. R. L. Lambrecht, and K. Kash, *Phys. Rev. B* **91**, 205207 (2015).
- T. Misaki, A. Wakahara, H. Okada, and A. Yoshida, *J. Cryst. Growth* **260**, 125 (2004).
- D. Skachkov and W. R. L. Lambrecht, *Phys. Rev. Mater.* **1**, 054604 (2017).
- S. Lyu, D. Skachkov, K. Kash, E. W. Blanton, and W. R. L. Lambrecht, *Phys. Status Solidi A* **216**, 1800875 (2019).
- D. Skachkov, A. P. Jaroenjittichai, L. Huang, and W. R. L. Lambrecht, *Phys. Rev. B* **93**, 155202 (2016).
- N. L. Adamski, Z. Zhu, D. Wickramaratne, and C. G. Van De Walle, *J. Appl. Phys.* **122**, 195701 (2017).
- H. C. Gatos and J. Lagowski, *J. Vac. Sci. Technol.* **10**, 130 (1973).
- L. Kronik and Y. Shapira, *Surf. Sci. Rep.* **37**, 1 (1999).
- H. Gao, S. Muralidharan, N. Pronin, M. R. Karim, S. M. White, T. Asel, G. Foster, S. Krishnamoorthy, S. Rajan, L. R. Cao, M. Higashiwaki, H. von



Wenckstern, M. Grundmann, H. Zhao, D. C. Look, and L. J. Brillson, [Appl. Phys. Lett.](#) **112**, 242102 (2018).

<sup>24</sup>D. Skachkov, P. C. Quayle, K. Kash, and W. R. L. Lambrecht, [Phys. Rev. B](#) **94**, 205201 (2016).

<sup>25</sup>S. Lany, A. N. Fioretti, P. P. Zawadzki, L. T. Schelhas, E. S. Toberer, A. Zakutayev, and A. C. Tamboli, [Phys. Rev. Mater.](#) **1**, 035401 (2017).

<sup>26</sup>E.W. Blanton, Ph.D. dissertation, Case Western Reserve University, 2016.

<sup>27</sup>T. Suehiro, M. Tansho, and T. Shimizu, [J. Phys. Chem. C](#) **121**, 27590 (2017).

<sup>28</sup>C. L. Melamed, M. B. Teliekamp, J. S. Mangum, J. D. Perkins, P. Dippo, E. S. Toberer, and A. C. Tamboli, [Phys. Rev. Mater.](#) **3**, 051602 (2019).